Spin morphologies and heat dissipation in spherical assemblies of magnetic nanoparticles

Manish Anand,[1] Julian Carrey,[2] and Varsha Banerjee[1]
[1]*Department of Physics, Indian Institute of Technology, Hauz Khas, New Delhi 110016, India*
[2]*Universite de Toulouse, INSA, UPS, Laboratoire de Physique et Chemie des Nano-Objects (LPCNO), 135 Avenue de Rangueil, F-31077 Toulouse, France*
(Received 27 May 2016; revised manuscript received 19 August 2016; published 21 September 2016)

Aggregates of magnetic nanoparticles (MNPs) exhibit unusual properties due to the interplay of small system size and long-range dipole-dipole interactions. Using the micromagnetic simulation software OOMMF, we study the spin morphologies and heat dissipation in micron-size spherical assemblies of MNPs. In particular, we examine the sensitivity of these properties to the dipolar strength, manipulated by the interparticle separation. As OOMMF is not designed for such a study, we have incorporated a novel scaling protocol for this purpose. We believe that it is essential for *all* studies where volume fractions are varied. Our main results are as follows: (i) Dense assemblies exhibit strong dipolar effects which yield local magnetic order in the core but not on the surface, where moments are randomly oriented. (ii) The probability distribution of ground-state energy exhibits a long high-energy tail for surface spins in contrast to small tails for the core spins. Consequently, there is a wide variation in the energy of surface spins but not the core spins. (iii) There is strong correlation between ground-state energy and heating properties on application of an oscillating magnetic field $h(t) = h_o \cos 2\pi f t$: the particles in the core heat uniformly, while those on the surface exhibit a wide range from cold to intensely hot. (iv) Specific choices of h_o and f yield characteristic spatial heat distributions, e.g., hot surface and cold core, or vice versa. (iv) For all values of h_o and f that we consider, heating was maximum at a specific volume fraction. These results are especially relevant in the context of contemporary applications such as hyperthermia and chemotherapy, and also for novel materials such as smart polymer beads and superspin glasses.

DOI: 10.1103/PhysRevB.94.094425

I. INTRODUCTION

Magnetic nanoparticles (MNPs) are attracting a lot of attention due to their tremendous potential in a variety of challenging applications [1–6]. These encompass biotechnology and biomedicine, therapeutics, engineering, material science, magnetic recording media, smart materials, etc. [7–11]. The main reason for their wide applicability is the ease with which they can be detected and manipulated by the application of an external magnetic field. They can be synthesized in varying sizes to yield application-tailored response time. Each application involves a unique exploitation of the MNPs and their properties. In therapeutics, for instance, they are targeted on malignant sites and subjected to an oscillating magnetic field. The magnetic moments undergo hysteresis, causing local warming. This effect is referred to as magnetic hyperthermia in the medical literature [7,12–15] and makes it possible to destroy cells or introduce a modest rise in temperature to increase the efficacy of chemotherapy. Consequently, recent years have evidenced intense investigations to achieve targeted and controlled heating for combating cancer.

Usually, MNPs with diameters $\lesssim$20 nm are single domain. They typically contain 10^3–10^5 magnetic moments locked together by the anisotropy energy to yield a *super*magnetic moment. The latter does not remain fixed in time, but undergoes fluctuations as it rotates between the crystallographic anisotropy axes even in the absence of an applied magnetic field. As a result, the time-averaged magnetization is still zero and the particle is *superparamagnetic*. When a large number of MNPs get sufficiently close to one another, the supermoments start interacting via dipole-dipole coupling. The latter has varied effects on systemic properties [16,17]. In some cases, the resulting dipolar field imparts a permanent magnetic moment to the assembly and creates an effectual ferromagnet. Further, these interactions are long range and allow for both ferromagnetic and antiferromagnetic couplings. So in some assemblies, these conflicting interactions cause frustration of spins, modify energy barriers, and impart spin-glass-like properties. Many studies have reported unconventional spin morphologies especially when the system size is smaller than the long range of dipolar interactions. Depending on the lattice structure, there have been observations of magnetic vortices, antiferromagnetic states, checkerboard patterns, etc. [18]. Consequently, they exhibit unusual ground-state and relaxation characteristics.

Aggregates of MNPs abound in nature. They also occur inadvertently in applications and are sometimes tailored to achieve required features. We provide below a few prototypical examples from distinct physical settings:

(a) Surprising concentrations of superparamagnetic magnetite (Fe_3O_4) nanoparticles ($\sim 10^8$) have been found in honey bees, homing pigeons, and dolphins. Chitons and magnetotactic bacteria also contain small magnetite particles, and can navigate with their help to the surface or bottom of the pools they live in [19,20]. It is natural to believe that these act as biological compasses for navigation. There has been much interest in them ever since their discovery.

(b) Lysosomes are the garbage disposal unit of a cell. Therefore they capture the targeted MNPs which form large compact aggregates containing 10^5–10^6 particles. When subjected to an oscillating magnetic field, there is sufficient rise in local temperature to permeabilize the lysosomal membrane, release degradative enzymes, and eventually cause cell death or apoptosis [21]. There is much to be understood in this recently discovered lysosomal cell-death pathway.

(c) Most conventional deposition techniques yield aggregates of nanoparticles. Recent studies have revealed that such assemblies exhibit *superferromagnetism* manifested in the form of hysteresis loops, return point memory, and unusually large heat dissipation [22–24]. A few others have observed a *super-spin-glass* phase analogous to the classical spin glass characterized by randomness and frustration [25,26].

(d) Smart polymer beads incorporating MNPs are being used for biosensing, targeted drug delivery, magnetic hyperthermia, etc. [8,9,27]. Their magnetoresponse (e.g., relaxation time, hysteresis, etc.) is closely related to the volume fraction of the nanoparticles which manipulates the dipolar strength.

(e) Ultra-high-density magnetic recording media store data as magnetization patterns in strips of densely packed single-domain *superparamagnetic* grains [11]. The interparticle interactions may impede the ability to address the single-particle magnetic response. A careful choice of the density of these grains is therefore required to obtain acceptable signal-to-noise ratio.

The above examples illustrate the emergence of collective behavior in closely packed superparamagnetic nanoparticles due to dipole-dipole interactions. It is therefore essential to identify parameters which manipulate these interactions in order to tailor the equilibrium and nonequilibrium properties of such aggregates. This is the primary focus of our work.

We consider spherical clusters of MNPs and study the interplay of the magnetic anisotropy, dipolar interactions, and packing fraction on spin morphologies and heating properties. The particles are arranged on a cubic lattice (with lattice constant a) inscribed in a sphere for simplifying the analysis. It is convenient to define a ratio $\Theta = D/KV$, where D is the strength of dipolar energy, K is the anisotropy constant, and V is the volume of the nanoparticle. The dipolar strength D has a $1/a^3$ dependence and can be varied with ease by changing the interparticle separation. We refer to $\Theta > 1$ as the strong dipolar regime and $\Theta \ll 1$ as the weak dipolar regime. Naturally, $\Theta = 0$ implies noninteracting magnetic spins. Our starting point is the Landau-Lifshitz (LL) equation to describe the precessional motion of a supermoment in a magnetic medium at $T = 0$. The coupled equations of motion are solved by the open-source software OOMMF (Object Oriented Micro Magnetic Framework) [28]. A scaling procedure has been introduced to correctly implement the effects of packing fraction in assemblies of MNPs. We have obtained numerical results for the commonly used magnetite ($Fe3O_4$) nanoparticles, but we believe that our observations are generic and hold for other kinds of MNPs as long as the value of Θ is comparable. To study the heating properties, we apply an oscillating magnetic field $H(t) = H_o \cos(2\pi f t)$, choosing the frequency $f = 10^7$, 10^8, and 10^9 Hz and the amplitude of the applied field $H_o = 0.2$, 0.4, and 0.6 T. These choices yield well-saturated loops. The main results of our study are as follows:

(1) In the strong dipolar regime ($\Theta \gtrsim 1$), the probability distributions $P(E)$ vs E of the ground-state energy of the MNPs are broad and asymmetric and with long high-energy tails. In the weak dipolar regime $\Theta < 1$, the distributions are peaked, symmetric, and have short tails. The average energy per spin $\bar{E}$ increases monotonically with Θ.

(2) In the strong dipolar regime, the spins in the core exhibit local magnetic order, but those at the periphery are randomly oriented. In the weak dipolar regime, all moments are randomly oriented. These impart unusual heating properties to the assemblies.

(3) In the strong dipolar regime, assemblies exhibit nonuniform heating; at low frequencies ($\sim 10^7$ Hz), the energy dissipated by the surface spins is nearly 40% more than by those in the core. The surface of the sphere is therefore hotter than the core. At the high frequencies ($\sim 10^9$ Hz), on the other hand, the core is hotter than the periphery.

(4) For all values of f and H_o, the heat dissipation is maximized at a critical interparticle separation a_c.

To explain the above results, we analyze the interplay between long-range dipolar interactions and system size, and identify experimental parameters which are responsible for it. In particular, our comprehension is useful to optimize the specific absorption rate (SAR) for hyperthermia and chemotherapy applications. Further, our observations made in the context of spherical aggregates are generic for suspensions, packed powders, and agglomerates of MNPs.

Many recent studies are emphasizing the need to include interparticle interactions for accurate estimation of heat dissipation and improved efficacy in hyperthermia procedures [29–35]. The starting point for theoretical understanding is a Hamiltonian incorporating dipole-dipole interactions. A variety of analytical and numerical methods such as mean-field approximation, linear response theory, kinetic Monte Carlo simulations (kMCS), and micromagnetic simulations has been used for analysis. An important piece of work in the context of our study is that by Tan *et al.* [21]. They use kMCS to study heating properties of iron-oxide nanoparticles in lysosomes. The primary findings of this work are (i) distinct spatial variation of heat as a function of the particle concentration and (ii) a nontrivial dependence of the specific absorption rate (SAR) on concentration. A few other studies have also investigated the role of dipolar interactions on SAR. Using a mean-field model, Landi has demonstrated that dipolar interactions increase the heating efficiency of *soft* magnetic particles but are detrimental for *hard* magnetic particles [36]. Haase and Nowak used the LL equation incorporating Langevin dynamics, and have reported that SAR decreases with increasing interactions [37]. Their observations agree with the more recent work of Ruta *et al.*, who used kMCS [38]. In an earlier work by the same group, Chantrell *et al.* studied the field-cooled and zero-field-cooled magnetization studies using kMCS [39]. They observe a state with short-range order at low temperatures in the assembly of MNPs with evidence of a transition to the glassy state. Note that the dipolar interactions are long range and fluctuate in sign. As a result, the energy landscape has many local minima separated by high barriers. These metastable states trap the evolving system and impede the relaxation to the equilibrium state. Our understanding of such complex systems therefore is far from complete.

This paper is organized as follows. In Sec. II, we introduce the model, the Landau-Lifshitz (LL) equation traditionally used to study spin dynamics of a single nanoparticle, and our adaptations to study interacting magnetic nanoparticle assemblies. In Sec. III, we study the role played by dipolar interactions on the organization of the supermoments and the

consequence of resulting spin morphologies on heating. In Sec. IV, we summarize our results and discuss them in the context of contemporary applications.

II. MODEL AND METHODOLOGY

Consider an assembly of N MNPs. Each particle has magnetic moment $\vec{\mu}_i = \mu\hat{e}_i$, $i = 1,2,\ldots,N$. The magnitude $\mu = M_s V$, where M_s is the saturation magnetization and V is the volume of the the nanoparticle. Further, we assume the particle to have uniaxial anisotropy $\vec{K} = K\hat{k}_i$, where K is the anisotropy constant and $\hat{k}_i$ is the direction of the anisotropy or the easy axis. As the nanoparticles are well separated, it is customary to assume that there is no exchange interaction between them [17,29,40]. The energy of such an assembly therefore includes contributions from the resulting magnetocrystalline anisotropy energy and the long-range dipole-dipole interactions [24,37]:

$$E = E_a + E_d = -KV\sum_{i=1}^{N}\cos^2\Phi_i - \frac{\mu_o\mu^2}{4\pi}\sum_{i,j}\frac{3(\hat{\mu}_i\cdot\hat{r_{ij}})(\hat{\mu}_i\cdot\hat{r_{ij}}) - (\hat{\mu}_i\cdot\hat{\mu}_j)}{r_{ij}^3}, \quad (1)$$

where μ_o is the permeability of free space, $\cos\Phi_i = \hat{k}_i\cdot\hat{e}_i$ is the angle between the anisotropy axis and the direction of the magnetic moment, r_{ij} is the distance between particles i and j, and $\hat{r_{ij}}$ is the vector along it. The radial dependence $1/r_{ij}^3$ means that the dipolar interaction is long range in nature and many more than nearest-neighbor interactions must be taken into account. The angular dependence implies that dipolar interaction can change sign, and hence the interaction switches from ferromagnetic for angles close to the easy axis to antiferromagnetic for intermediate angles ($55^\circ \leqslant \theta_{ij} \leqslant 125^\circ$). Thus there are competing ferro- and antiferromagnetic interactions.

Expressing the distance in units of the lattice parameter a, Eq. (1) can be rewritten as

$$E = -KV\sum_{i=1}^{N}\cos^2\Phi_i - D\sum_{i,j}\frac{3(\hat{\mu}_i\cdot\hat{r_{ij}})(\hat{\mu}_i\cdot\hat{r_{ij}}) - (\hat{\mu}_i\cdot\hat{\mu}_j)}{(r_{ij}/a)^3}, \quad (2)$$

where we define the *dipolar constant* $D = \mu_o\mu^2/4\pi a^3$. The behavior of such an assembly is governed by the relative strengths of the anisotropy energy and the dipolar energy. It is therefore convenient to define a ratio $\Theta = D/KV$. Note that for a given value of the latter, there can be many combinations of (K,μ,a). Said differently, it is possible to tailor Θ by choosing an appropriate triplet which can be manipulated in experiments. For example, a change in size of the constituting nanoparticles can alter V, replacing the magnetic material with another can alter μ and K, and a variation of the volume fraction can alter a. We emphasize, however, that the properties of the assembly will be dictated by Θ rather than the precise parameter values. In the rest of our discussion, we refer to $\Theta > 1$ as the strong dipolar regime and $\Theta \ll 1$ as the weak dipolar regime.

If an external magnetic field $\vec{H}(t)$ is applied, there is an additional contribution to Eqs. (1) and (2) given by [37]

$$E_H = -\vec{H}\cdot\sum_{i=1}^{N}\vec{\mu}_i = -M_s V\vec{H}\cdot\sum_{i=1}^{N}\hat{e}_i. \quad (3)$$

In hysteresis studies, an oscillating magnetic field is applied in a suitable direction. In this case, $H \equiv H(t) = H_o\cos(2\pi f t)$, where H_o is the amplitude and f is the frequency of the applied field.

The precessional motion of the magnetic moment $\vec{\mu}_i$ in a magnetic background is described by the Landau-Lifshitz (LL) equation. It predicts the rotation of the magnetization in response to torques and is given by [37,41]

$$\frac{d\vec{\mu}_i}{dt} = -\gamma\vec{\mu}_i\times\vec{H}_i^e - \lambda\vec{\mu}_i\times\left(\vec{\mu}_i\times\vec{H}_i^e\right), \quad i = 1,2,\ldots,N, \quad (4)$$

where γ is the Landau-Lifshitz gyromagnetic ratio, $\lambda = \gamma\alpha/M_s$ is a phenomenological dimensionless damping factor representing all relaxational mechanisms, and $\vec{H}_i^e = -\partial(E + E_H)/\partial\vec{\mu}_i$ is the effective field experienced by magnetic moment due to the surrounding magnetic medium. The first term in Eq. (4) describes the precession of $\vec{\mu}_i$ around $\vec{H}_i^e$. The second term describes a phenomenological dissipative motion: the magnetic moment $\vec{\mu}_i$ precesses around $\vec{H}_i^e$, loses energy to the environment in accordance with the damping factor λ, and eventually (at $t\to\infty$) aligns along the effective field. The coupled differential equations in Eq. (4) are usually solved using integrators such as OOMMF [42] or NMAG [43] to obtain the ($T = 0$) ground-state morphology which yields the organization of the supermoments in the assembly. In these procedures, the simulated nanoparticle is comprised of cells with, say, lateral dimension l. Each cell then represents a magnetic moment $\mu = M_s V$, where the volume $V = l^3$. The center-to-center separation between moments is therefore $l \equiv a_0$.

At this juncture, it is useful to discuss the evaluation of E_a, E_d, and E_H in micromagnetic simulations. The discrete forms in Eqs. (1)–(3) need to be rewritten for use in the LL equation. In 1963, Brown suggested that instead of considering individual magnetic moments, it is appropriate for this purpose to use a continuous magnetization function $\mathbf{M}(\mathbf{r})$ representing a local average [44]:

$$\mathbf{M}(\mathbf{r}) = \frac{1}{V(r,\Delta r)}\sum_{i\,\in\,\mathcal{I}(\mathbf{r},\Delta r)}\vec{\mu}_i, \quad (5)$$

where $V(r,\Delta r)$ is a sphere of radius Δr placed at $\mathbf{r}$ and $\mathcal{I}(\mathbf{r},\Delta r)$ refers to the set of indices i which lie in this sphere. $\mathbf{M}(\mathbf{r})$ is assumed to be continuous and differentiable. In terms of this locally averaged magnetization density, the anisotropy energy is [42,45]

$$E_a = -\int_V K(r)(\hat{k}\cdot\hat{e})^2 d^3r. \quad (6)$$

Similarly, the dipolar energy or the *demagnetization energy* can be expressed as [42,44–47]

$$E_d = -\frac{\mu_o}{2}\int_V \mathbf{M}(\mathbf{r})\cdot\mathbf{H_d}(\mathbf{r})d^3r, \tag{7}$$

where the demagnetization field $\vec{H}_d$ at position r contains components contributed from the divergence of magnetization within the volume and surface poles,

$$\mathbf{H_d}(r) = -\frac{1}{4\pi}\int_V \vec{\nabla}\cdot\mathbf{M}(\mathbf{r}')\frac{\mathbf{r}-\mathbf{r}'}{|\mathbf{r}-\mathbf{r}'|^3}d^3r' + \frac{1}{4\pi}\int_S \hat{n}\cdot\mathbf{M}(\mathbf{r}')\frac{\mathbf{r}-\mathbf{r}'}{|\mathbf{r}-\mathbf{r}'|^3}d^2\mathbf{r}', \tag{8}$$

where $\hat{n}$ is the surface normal. Finally, the Zeeman energy becomes [42]

$$E_H = -\frac{\mu_o}{2}\int_V \mathbf{M}\cdot\mathbf{H}(\mathbf{r})d^3r. \tag{9}$$

As $\mathbf{M}(\mathbf{r})$ is continuous and differentiable at least within each cell, the discrete approximations can be recovered from a Taylor expansion of the relevant equations keeping terms up to the second order. Higher-order terms get incorporated in Eq. (8) if dipole-quadrupole or quadrupole-quadrupole interactions are significant. The details of these derivations can be found in [42]. It should be noted that the dipolar energy E_d involves long-range interactions and, in terms with $\mathbf{M}$, requires integration over $V \times V$. Computationally, it is the most expensive calculation.

The main goal of our work is to investigate the role played by the dipolar-dipole interaction on morphologies and heating of the magnetic nanoparticle assemblies. By our formulation in Eq. (2), the strength of the dipolar interaction can be manipulated by the center-to-center separation a of the MNPs. Note, however, that with the protocol used in OOMMF, a change in the center-to-center separation from a_0 to a_α, say, is tantamount to changing the cell volume from $V \equiv V_0\ (= a_0^3)$ to $V_\alpha\ (= a_\alpha^3)$. Consequently, the magnetic moment gets altered to $\mu_\alpha = M_s V_\alpha$, thereby modifying the magnetic properties of the particles under study. This undesirable artifact in the simulation needs to be overcome. We do so by a simple rescaling of the saturation magnetization,

$$M_s^\alpha = M_s^0\frac{V_0}{V_\alpha}, \tag{10}$$

where M_s^0 is the saturation magnetization for a particle of volume $V_0 = a_0^3$. It is easy to see that now $\mu = M_s^0 V_0 = M_s^\alpha V_\alpha$, as desired. Corresponding changes need to be incorporated in other related variables such as the coercive field $H_c = K/M_s$ [12] and the anisotropy field $H_K = 2K/M_s$ [12], which play an important role in hysteresis and heat dissipation:

$$H_c^\alpha = H_c^0\frac{V_\alpha}{V_0}, \tag{11}$$

$$H_K^\alpha = H_K^0\frac{V_\alpha}{V_0}. \tag{12}$$

One signature of the correctness of the scaling protocol described by Eqs. (10)–(12) is a *master collapse* of hysteresis loops. We demonstrate this for Fe_3O_4 and Co nanoparticle assemblies in the forthcoming section. We also make comparisons with corresponding data from kMCS, the alternative approach to study complex spin systems. A convergence between them should reinforce the need for the variable scaling introduced in Eqs. (10)–(12).

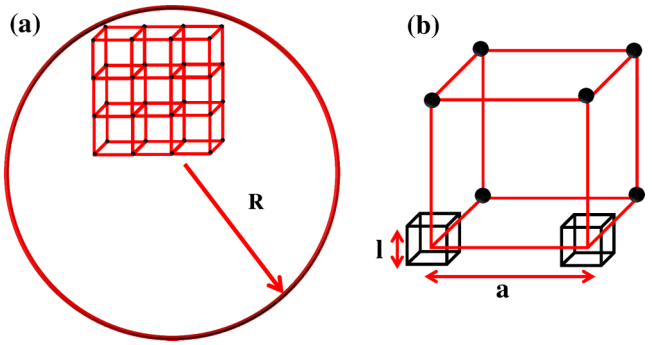

FIG. 1. (a) Schematic of the sphere of radius R containing cubic MNPs with lateral dimension l arranged on a lattice with spacing a. (b) Enlarged portion of the basic unit cell in (a).

III. SIMULATION RESULTS

Consider the schematic in Fig. 1, which depicts a sphere of radius R packed with MNPs. For simplicity, we assume that they are cubes with a lateral dimension l and are arranged on the vertices of a simple cubic lattice with spacing a. The center-to-center separation between the particles is a, while the edge-to-edge separation is $a - l$. Most applications use Fe_3O_4, Co, and Fe_2O_3 nanoparticles. Table I provides values of the saturation magnetization M_s and anisotropy constant K for these materials [48]. We perform simulations using OOMMF for the geometry depicted in Fig. 1 for cubic particles with $l = 10$ nm and $R = 200$ nm using free boundary conditions. Typically, the damping constant α lies in the interval [0,1]. Without loss of generality, we choose $\alpha = 1$. The initial condition is chosen to be a random orientation of magnetization and anisotropy axes of each packed particle. The magnetic field H has been applied along the z direction. All data have been averaged over 50 independent initial conditions. Most of our results are for Fe_3O_4 nanoparticles. We have also performed evaluations for Co and Fe_2O_3 nanoparticles, and for other sets of l and R. Our simulations indicate that the results remain qualitatively unchanged provided the value of Θ is the same. A few words of caution are required for discretization of noncuboid geometries such as spheres, cones, cylinders, rings, etc. [49]. On the one hand, it should not be so fine that the computational time becomes unreasonably large. On the

TABLE I. List of parameters used in numerical evaluations.

K (Fe_3O_4)	1.3×10^4 J m^{-3}
K (Co)	4.10×10^5 J m^{-3}
K ($\alpha - Fe_2O_3$)	7.0×10^3 J m^{-3}
M_s (Fe_3O_4)	4.77×10^5 A m^{-1}
M_s (Co)	1.44×10^6 A m^{-1}
M_s ($\alpha - Fe_2O_3$)	2.39×10^3 A m^{-1}

other hand, it should not be so coarse grained that the system exhibits incorrect physical behavior. To eliminate such doubts, we converge on the optimal cell size only after comparing our results with corresponding kinetic Monte Carlo outcomes from the literature whenever possible. The rule of thumb is to ensure that the fraction of moments on the surface is much smaller than those in the bulk [49]. For example, when $R = 200$ nm and $l = 10$ nm, the number of cells on the surface is ∼3700, while that in the bulk is ∼30 000.

A. Checks for proposed scaling

We perform hysteresis loop calculations for assemblies of (i) Fe_3O_4 and (ii) Co nanoparticles with $l = 10$ nm for five values of the interparticle separation: $a_0 = 10$, $a_1 = 14$, $a_2 = 16$, $a_3 = 20$, and $a_4 = 50$ nm.

Using the value of M_s^0 and K from Table I, the saturation magnetization M_s^α for subsequent separations was obtained by the scaling in Eq. (10). The corresponding H_c^α and H_K^α were calculated using Eqs. (11) and (12), respectively. We chose H_o^α to be $\gtrsim 4H_c^\alpha$ to obtain well-saturated loops. The frequency of the applied oscillating field f was chosen to be 10^7 Hz. The assembly was allowed to undergo a few field cycles for the transients to settle down.

The equilibrated hysteresis loops for (i) Fe_3O_4 and (ii) Co MNP assemblies are presented in Fig. 2. The values of H_o^α used for each value of a_α are also specified. The x axis has been scaled by the anisotropy field H_K and the y axis by the saturation magnetization M_s. The solid black curve depicts the equilibrated hysteresis loop of a single particle, i.e., when $a = \infty$. We have generated this data set by performing kMCS for a single Fe_3O_4 particle subjected to a time-varying field of frequency $f = 10^7$ Hz. The kMCS procedure that we have used is described in detail in Ref. [21] and is not reiterated here for the sake of brevity. The data collapse is excellent for both sets of particles even when they are closely spaced. For example, in the case of Fe_3O_4, a separation of 14 nm exhibits a good collapse. From Table II, it corresponds to $\Theta \simeq 0.63$, implying significant strength of dipolar interactions. Our checks reveal that this agreement is absent if the scaling protocol is not employed, lending credence to Eqs. (10)–(12).

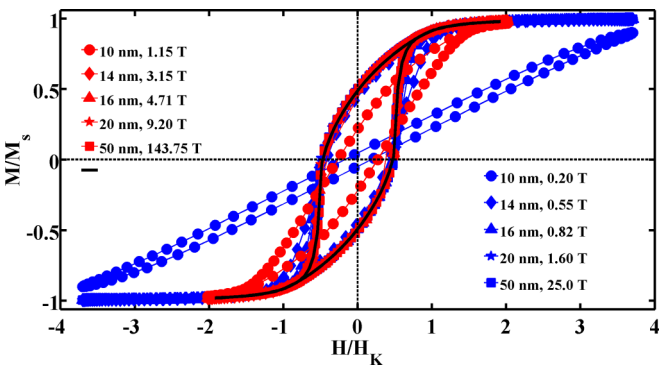

FIG. 2. Scaled hysteresis loops (refer to text) corresponding to assemblies of Fe_3O_4 nanoparticles in blue (black) symbols and Co nanoparticles in red (gray) symbols for indicated values of the lattice spacing a and field strength H_o. The frequency of the applied field $f = 10^7$ Hz. The solid black curve is for $a = \infty$ corresponding to a noninteracting assembly of MNPs. This data has been obtained using kMCS as detailed in the text.

TABLE II. Evaluation of the ratio $\Theta = D/KV$ as a function of center-to-center interparticle separation a for cubic particle of three commonly used magnetic compositions. The lateral dimension of the particle $l = 10$ nm in each case.

	$\Theta = D/KV$		
a (nm)	Fe_3O_4	Co	$\alpha - Fe_2O_3$
10	1.75	0.42	8.2×10^{-5}
11	1.32	0.34	6.3×10^{-5}
12	1.01	0.24	4.7×10^{-5}
14	0.62	0.15	3.0×10^{-5}
16	0.42	0.10	2.0×10^{-5}
20	0.22	0.05	1.2×10^{-5}
30	0.06	0.02	3.0×10^{-6}
40	0.03	0.01	1.3×10^{-6}
50	0.01	0.0034	6.5×10^{-7}
100	0.001	0.0004	8.2×10^{-8}

We emphasize that they are essential for the correct implementation of OOMMF when probing the influence volume fraction (and thereby dipolar effects) on the behavior of assemblies of MNPs.

B. Ground-state morphologies

Next we study ($T = 0$) spin morphologies of the spherical assemblies as a function of the interparticle separation. Figure 3 depicts the ground-state ($T = 0$) morphology for lattice spacing of (a) $a = 10$ and (b) $a = 20$ nm. These correspond to $\Theta \simeq 1.75$ and $\Theta \simeq 0.22$, respectively. The morphology in Fig. 3(a) contains 33 496 MNPs, while that in Fig. 3(b) contains 4186 MNPs. The corresponding slices taken at $z = 0$ in the xy plane are provided below in Figs. 3(c) and 3(d). Notice that for the strong dipolar case, there is local magnetic order. In the weak dipolar case, however, the moments are oriented randomly, indicating absence of magnetic order. To probe further, we plot the average values of the components of the magnetic moment $\overline{\mu}_x$, $\overline{\mu}_y$, and $\overline{\mu}_z$ as a function of r/a, the distance from the center of the sphere in units of the interparticle separation in Figs. 3(e) and 3(f). Note that the averaging at the center is over a much fewer number of moments. For example, in Fig. 3(e), when $r = 10$ nm, there are 8 moments in the shell. So the corresponding data points are averaged over 400 moments (8 neighbors, 50 initial conditions). The number of moments contributing to the average increases rapidly as we move away from the center. For example, for $r = 20$, 50, and 200 nm, the averaging is over $\sim 10^3$, 10^4, and 10^5 moments, respectively. We have therefore shown in the figures only those data points which have been averaged over 10^3 values or more for reliability of results. In Fig. 3(e), where $\Theta \simeq 1.75$, there is significant local magnetic order in the interior of the sphere but not near the surface. In Fig. 3(f), where $\Theta \simeq 0.22$, there are signs of weak ordering in the interior which is rapidly destroyed as the surface of the sphere is approached.

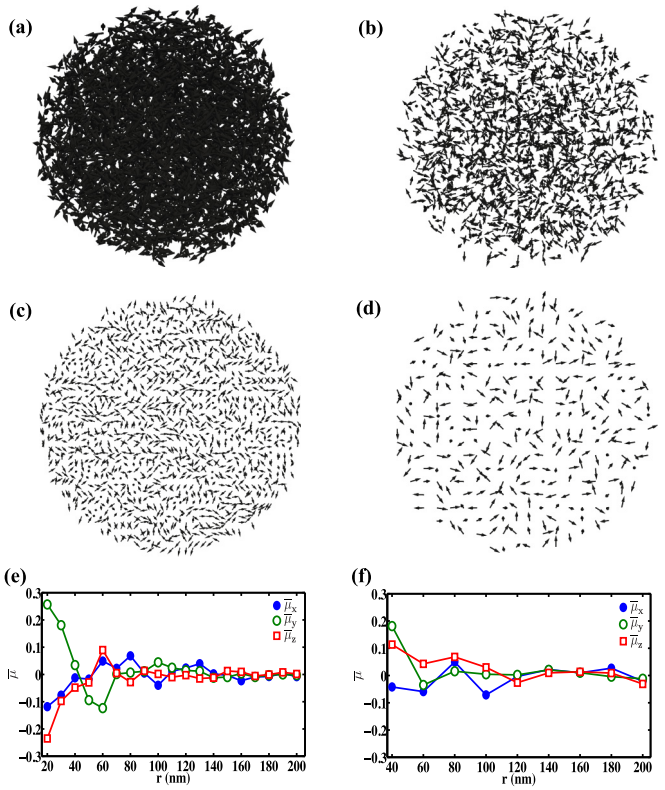

FIG. 3. Typical ground-state morphologies of Fe_3O_4 nanoparticles ($l = 10$ nm) assembled in a sphere of radius $R = 200$ nm on a cubic lattice with spacing (a) $a = 10$ nm corresponding to $\Theta \simeq 1.75$ and (b) $a = 20$ nm corresponding to $\Theta \simeq 0.21$. The morphology in (a) contains 33 496 MNPs, while that in (b) contains 4186 MNPs. The slices in (c) and (d) are taken at $z = 0$ in the xy plane. The average value of the component of the magnetic moment $\overline{\mu}_i$ vs r for (e) $a = 10$ nm and (f) $a = 20$ nm is also indicated. The data have been averaged over $\sim 10^3$ values for $r = 20$ nm and $\sim 10^5$ values for $r = 200$ nm.

One reason for surface effects in the strong dipolar regime is the influence of the long-range nature of dipolar interactions. In this context, it is useful to study Fig. 4 which depicts the variation of Θ as a function of r/a for cubic Fe_3O_4 particles with $l = 10$ nm. The two data sets are for $a = 10$ and 20 nm. The integer values $n = r/a$ can be interpreted as the nth neighbor of the moment placed at $r/a = 0$. Note that Θ is the largest when $a = l$, which corresponds to 10 nm in the present case. The inset shows a magnified view for $r/a \geqslant 5$. For $\Theta > 1$, the dipolar effects continue to be significant at large distance ($r/a \simeq 10$). Therefore, the moments in the core have a dipolar exchange with a large number of spins vis a vis the surface spins, which have no neighbors at the outside. Consequently, the interior spins are under the influence of an effective *mean* dipolar field, while the surface spins experience wide deviations from it.

To gain further understanding of the effects of long-range dipolar interactions, we analyze the ground-state energy E for the morphologies in Fig. 3. In Figs. 5(a) and 5(b), we plot the corresponding probability distribution $P(E)$ vs E. The average energy $\overline{E}$ is also specified for comparison. Notice that $\overline{E}$ for the strong dipolar case ($a = 10$ nm, $\Theta \simeq 1.7$) is an order

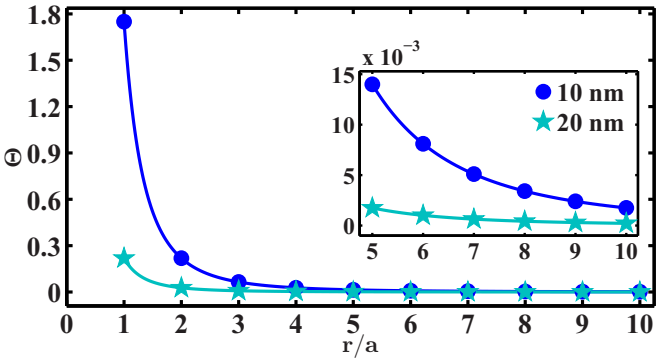

FIG. 4. Variation of $\Theta = D/KV$ for cubic Fe_3O_4 nanoparticles with $l = 10$ nm as a function of r/a, where r is the center-to-center distance between two particles and a is the spacing of the underlying lattice. The data sets are for $a = 10$ and 20 nm. The inset shows a magnified view for $r/a \geqslant 5$, i.e., for the fifth neighbor and beyond. For $\Theta > 1$, the dipolar effects continue to be significant even beyond $r/a = 10$ or the tenth neighbor. Note that Θ is the largest when $a = l$, which corresponds to 10 nm in the present case.

of magnitude larger than that for the weak dipolar case ($a = 20$ nm, $\Theta \simeq 0.2$). In general, $\overline{E}$ increases monotonically with Θ. In the strong dipolar regime, the distribution is asymmetric with a long tail, indicating the presence of sites with magnetic energy nearly five times the average. In the weak dipolar regime, the distribution is well peaked and with a shorter tail. To probe the connection between these distributions and the spin morphologies, we show in Figs. 5(c) and 5(d) the energy distributions $P_s(E)$ vs E for MNPs in concentric spherical shells of specified radii. It can be observed that for $\Theta \simeq 1.7$, the outermost shell has a distinctly wide distribution with a long tail. Checks of the variance indicated that the energy of the majority of spins in the inner shells is close to the average value $\overline{E}_s$. The influence of dipolar interactions on surface spins is further reinforced in Figs. 5(e) and 5(f), where we plot the variation of $\overline{E}_s$ as a function of the shell radius. The y axis is scaled by the maximum value E_m ($\equiv \max\{\overline{E}_s\}$) to facilitate relative comparison of the energies of the different shells. Clearly, for the $\Theta \simeq 1.7$ case, there are strong surface effects. These have important implications for hysteresis and heating, as we shall see in the forthcoming section.

C. Heat dissipation

To study heat dissipation, the morphologies in Fig. 3 were subjected to an oscillating magnetic field $H = H_o \cos(2\pi f t)$. We have used three different values of H_o: 0.2, 0.4, and 0.6 T; and three different values of f: 10^7, 10^8, and 10^9 Hz. These parameters resulted in well-saturated hysteresis loops. The assemblies were allowed to undergo a few field cycles to remove the transients prior to obtaining well-equilibrated loops. We then calculated heat dissipated by evaluating the loop area $E_H^i \equiv A_i = \oint \mu_i \cdot dH$, $i = 1,2,\ldots,N$. As before, all the data that we present are averaged over 50 initial conditions.

In Fig. 6, we present representative results of heat dissipated by the MNPs subject to the following conditions: $a = 10$ nm, $H_o = 0.4$ T, $f = 10^7$ Hz [Fig. 6(a)]; $a = 10$ nm,

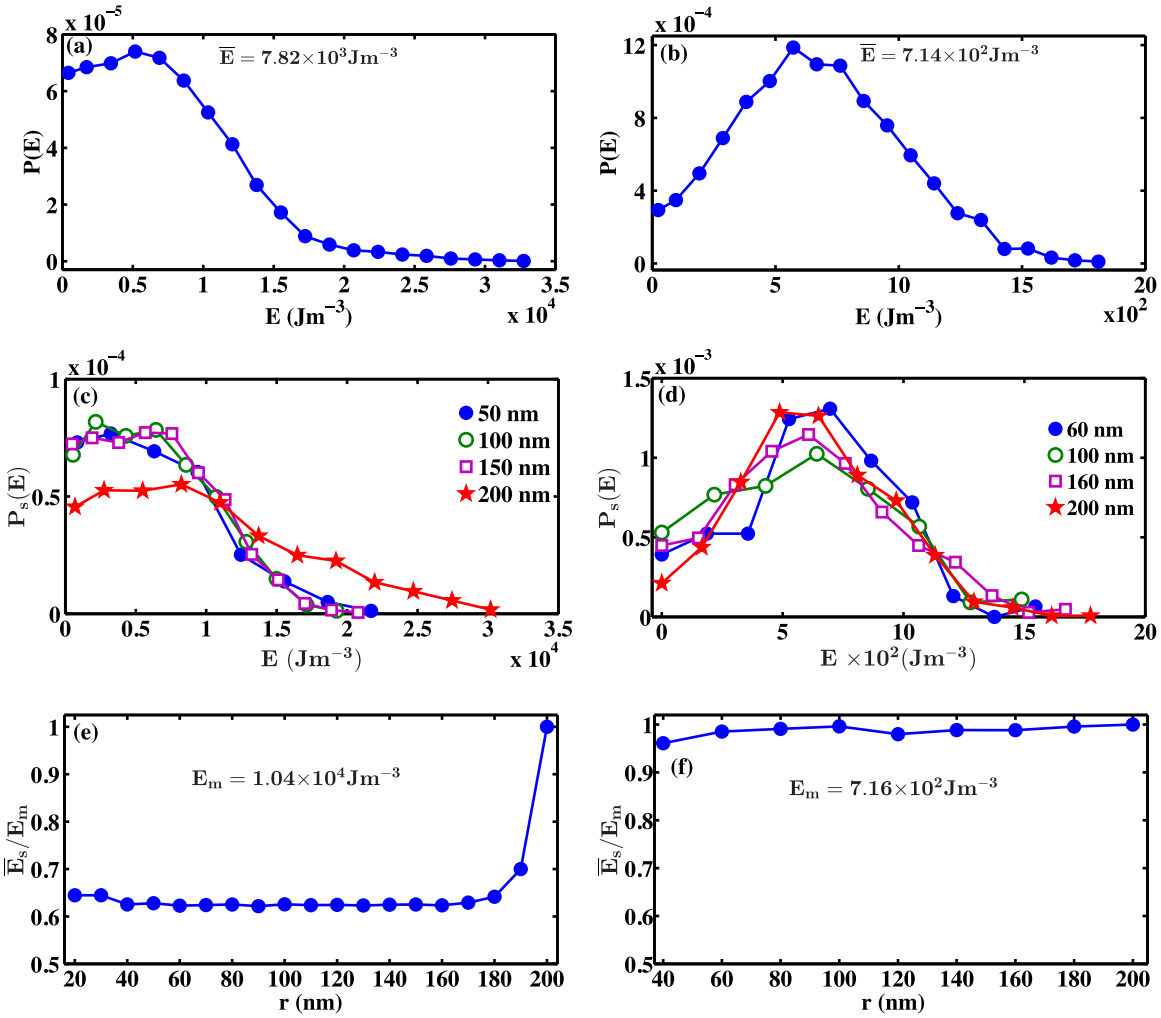

FIG. 5. Probability distributions $P(E)$ vs E of the ground-state energy for Fe_3O_4 MNPs packed in a sphere of radius $R = 200$ nm for lattice spacing (a) $a = 10$ nm and (b) $a = 20$ nm. These values of a correspond to $\Theta \simeq 1.7$ and 0.2, respectively. (c),(d) The corresponding probability distribution of energy $P_s(E)$ vs E for MNPs in concentric spherical shells of specified radii. (e),(f) The variation of the average energy of a nanoparticle in the shell $\overline{E}_s$ vs r. The y axis has been scaled by the maximum value E_m to enable comparisons. Clearly, there are strong surface effects for the $\Theta \simeq 1.7$ case.

$H_o = 0.4$ T, $f = 10^9$ Hz [Fig. 6(b)]; $a = 20$ nm, $H_o = 0.4$ T, $f = 10^7$ Hz [Fig. 6(c)], and $a = 20$ nm, $H_o = 0.4$ T, $f = 10^9$ Hz [Fig. 6(d)]. The corresponding 2-d slices are indicated in Figs. 6(e)–6(h), respectively. The color charts are a measure of the heat dissipated in J m^{-3}. Notice that the compact, strongly interacting assembly ($a = 10$ nm $= l$, $\Theta \simeq 1.7$) in Fig. 6(a) exhibits nonuniform heating, with the surface significantly warmer than the core.

Before examining spatially distributed heating in detail, we demonstrate the convergence between results obtained from OOMMF and kMCS. Figure 7 shows the probability distribution $P(E_H)$ vs E_H of the heat dissipated in spherical assemblies of Fe_3O_4 MNPs with 10 and 20 nm separations using (a) OOMMF (blue symbols) and (b) kMCS (red symbols). The axes have been scaled by the average energy $\overline{E}_H$ and both data sets have been averaged over 50 initial conditions. There is good qualitative agreement between the two data sets. Recall that evaluations in OOMMF are at $T = 0$, unlike the kMCS which are at $T \neq 0$. At this juncture, a few words about the phenomenological rate constant λ in Eq. (4) are also in order. It represents the coupling of the magnetic moment $\vec{\mu}$ to a heat bath. According to Brown, it can be interpreted as a statistical average of the rapidly fluctuating random forces due to thermal agitation [44,50]. Thus although λ captures the effects of temperature, the form of the relationship is unknown in the LL formulation. However, at sufficiently high temperatures, close to the ferromagnetic-paramagnetic transition, thermal effects can be precisely taken into account using the Langevin dynamics [50–52].

To systematically analyze the nonuniform heating in morphologies, we plot in Figs. 8(a)–8(d) the corresponding probability distribution $P_s(E_H)$ vs E_H of the MNPs in different shells of specified radius. The Figs. 8(e) and 8(f) indicate the variation of the average energy of a particle as a function of the shell radius $\overline{E}_s/E_m$ vs r. Recall that all data near the surface of the sphere are averaged over 10^5 values. So our numerics at the periphery are very accurate. The distinct spatial heat distribution for each parameter set is captured well in

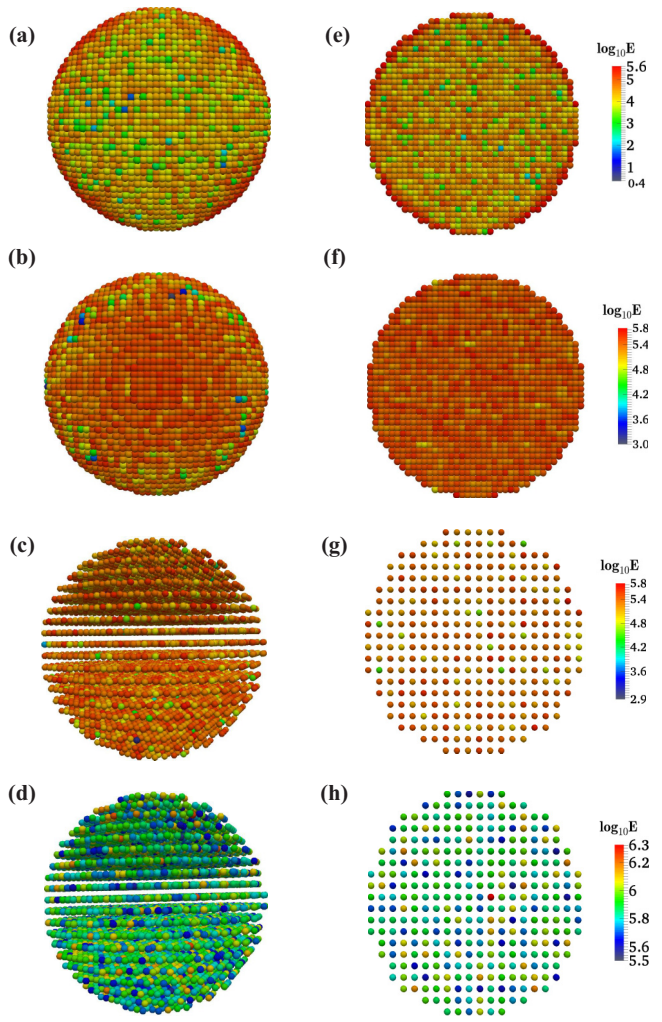

FIG. 6. Heat dissipated in MNP spheres on application of the oscillating field $H = H_o \cos 2\pi f t$ indicated by corresponding color charts in J m^{-3}. The interparticle separation in the left panel is 10 nm, while that in the right panel is 20 nm. The distinct parameters are (a) $a = 10$ nm, $H_o = 0.4$ T, $f = 10^7$ Hz; (b) $a = 10$ nm, $H_o = 0.4$ T, $f = 10^9$ Hz; (c) $a = 20$ nm, $H_o = 0.4$ T, $f = 10^7$ Hz; and (d) $a = 20$ nm, $H_o = 0.4$ T, $f = 10^9$ Hz. The corresponding 2-d slices are indicated, respectively, in (e)–(h).

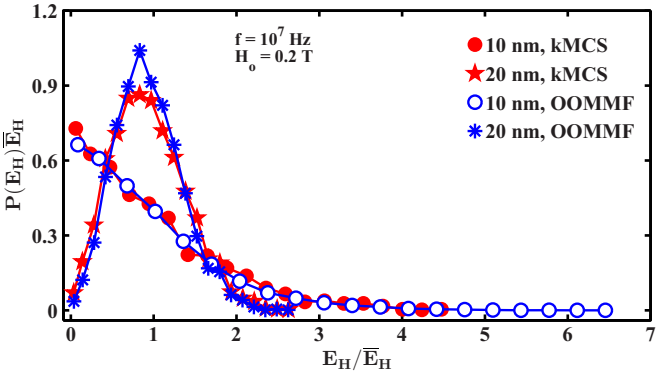

FIG. 7. Probability distribution $P(E_H)$ vs E_H of heat dissipated by MNPs for $a = 10$ and 20 nm from OOMMF in blue (black) symbols and kMCS in red (gray) symbols. The field strength $H_o = 0.2$ T and the frequency $f = 10^7$ Hz.

Fig. 9, which is the pictorial representation of Figs. 8(a)–8(d). The innermost shell has been left uncolored because the corresponding data have been averaged over lesser values ($<10^3$).

The important conclusions that can be drawn from Figs. 8 are the following: (i) In the strong dipolar regime ($\Theta \simeq 1.7$) for lower frequencies ($f \sim 10^7$), the heat dissipated by surface spins is spread across four orders of magnitude, ranging from 0 to 10^4 J m^{-3}. Locally, there are a few scattered intensely hot spots. Globally, the peripheral surface is hotter than the core by approximately 40%. (ii) For higher frequencies ($f \sim 10^9$), the distributions $P_s(E_H)$ vs E_H are well peaked and symmetric. The peak of the distribution and the mean value $\overline{E}_s$ of the outermost shell is the smallest. This surface behavior yields a cooler periphery than the core by approximately 8%. (iii) In the weak dipolar regime ($\Theta \simeq 0.2$), $P_s(E_H)$ vs E_H is well peaked with the same qualitative form for all the shells. These assemblies exhibit uniform heating at all values of frequency and field.

In the context of the above observations, we mention that Tan *et al.* also observed spatially distributed heating in lysosomes containing iron-oxide nanoparticles for an applied field of frequency $f = 10^5$ Hz and amplitude $H_o = 0.04$ T [21]. They used kMCS performed at $T = 300$ K. A hot surface and cold core were observed for a high-volume fraction (3% or more) and vice versa for those with low-volume fractions ($\simeq$0.6%). Our results are in qualitative agreement with these observations for the dense-packing and low-frequency case of Fig. 6(a) and the corresponding schematic in Fig. 9(a). We cannot compare the other cases because the study by Tan *et al.* and other studies as well have not probed the frequency dependence of heating. The spatially distributed heating is therefore a robust property observed at $T \neq 0$ in aggregates of MNPs for a suitable choice of field parameters.

Finally, in Fig. 10, we show the variation of the hysteresis loop area as a function of a. The latter is varied from 10 nm, corresponding to dipolar strength $\Theta \simeq 1.7$, to 100 nm, corresponding to $\Theta \simeq 0$. The amplitude H_o of the applied field is 0.2 T [Fig. 10(a)], 0.4 T [Fig. 10(b)], and 0.6 T [Fig. 10(c)]. Each set contains evaluations for three values of the frequency $f = 10^7, 10^8$, and 10^9 Hz. As before, the scaling forms in Eqs. (10)–(12) were used to obtain correct values of M_s, H_c, and H_K. All data clearly indicate that maximum heat dissipation occurs at a critical separation a^* and not at $a = l$ which maximizes Θ. Our results are in agreement with observations made by Tan *et al.* [21], Haase and Nowak [37], and Ruta *et al.* [38], but not with that of Landi [36].

IV. DISCUSSION AND CONCLUSION

The nonequilibrium relaxation in complex spin systems can be interpreted in terms of a phenomenological model with a complicated free-energy surface having several metastable minima [53,54]. They differ from each other by small groups of spins and are separated by randomly distributed barriers. In the absence of an external field, there is a distribution of barrier heights (Δ) and a corresponding distribution of escape (relaxation) times from these minima ($\tau_e \sim e^{\beta\Delta}$). As a consequence, there is frequent trapping of the system in local minima. When an oscillating magnetic field $H(t) = H_o \cos(2\pi f t)$ is applied,

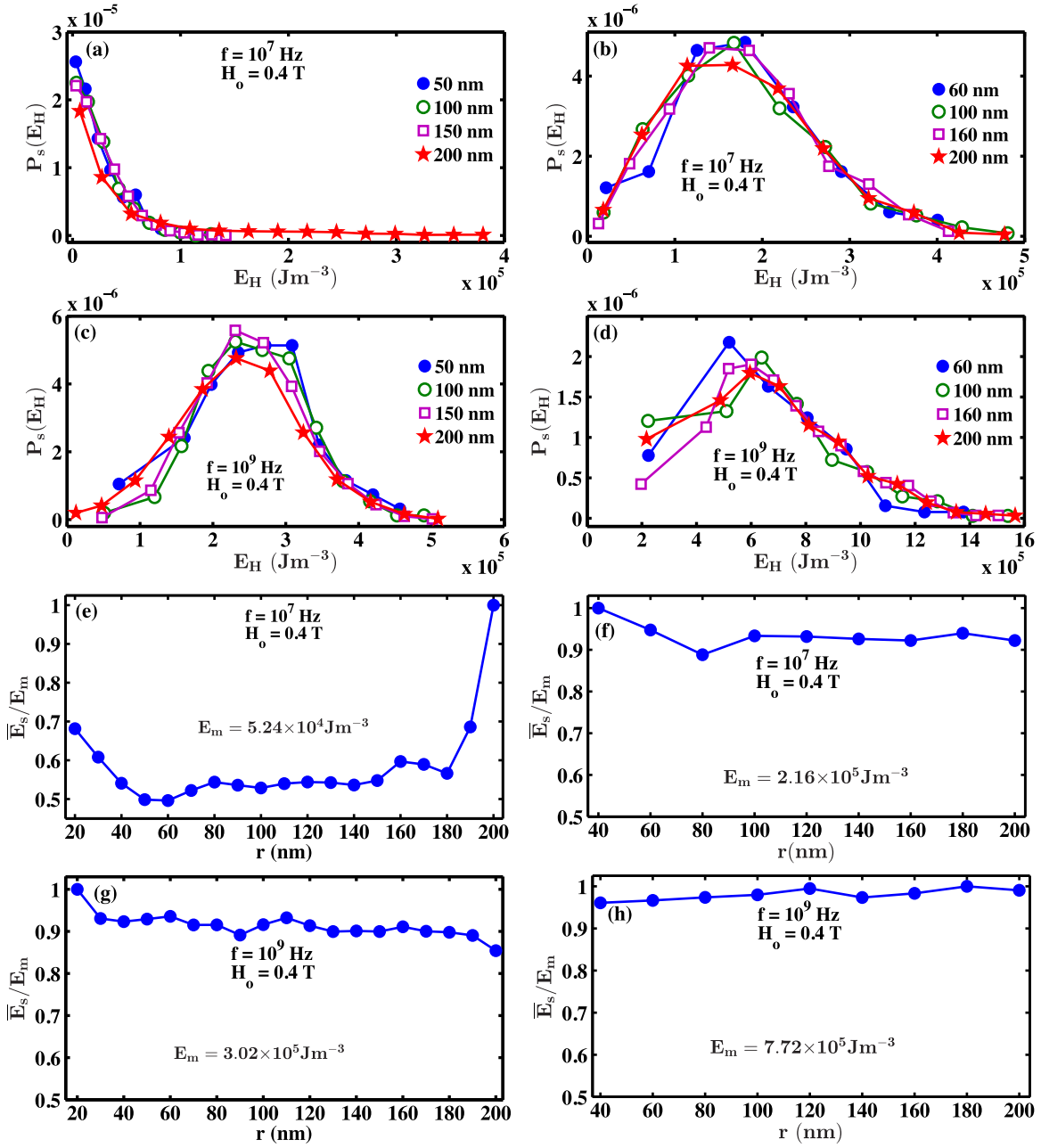

FIG. 8. Probability distribution of heat dissipation $P_s(E_H)$ vs E_H for MNPs in concentric spherical shells of specified radii for (a) $a = 10$ nm, $H_o = 0.4$ T, $f = 10^7$ Hz; (b) $a = 20$ nm, $H_o = 0.4$ T, $f = 10^7$ Hz; (c) $a = 10$ nm, $H_o = 0.4$ T, $f = 10^9$ Hz; and (d) $a = 20$ nm, $H_o = 0.4$ T, $f = 10^9$ Hz. (e)–(h) Corresponding variation of $\overline{E}_s$ vs r. The y axis has been scaled by E_m for comparison. Note that the data points at the periphery are averaged over 10^5 values and are very accurate.

the response of the system is delayed, leading to hysteresis. The nature of the response is determined by the competition between experimental time scales (measured by the inverse frequency of the applied perturbation) and the relaxation time scale. Typically, $\tau_e \ll f^{-1}$ corresponds to the low-hysteresis limit, as the spins readjusts to the applied field before it changes substantially. For magnetic field strengths $H_o \geqslant \Delta$, we expect that the escape times which are relevant to spin dynamics in an oscillatory magnetic field satisfy $f^{-1} > \tau_e$. If $H_o \ll \Delta$, the dipolar effects are dominant and temporal evolution occurs primarily through thermally activated barrier hopping.

What happens to the above scenario in the small spherical aggregates of MNPs? At $T = 0$, the moments align along the local effective field $h_i^e = -\partial E/\partial \mu_i$, where $E = E_a + E_d$ from Eq. (1). The dipole-dipole interactions, however, introduce frustrations in the moments, which lead to deep valleys separated by barriers in the energy function. The approach to the ground state is impeded by the local minima and the system then opts for a metastable state. Now consider the application of the oscillating field $H(t) = H_o \cos(2\pi f t)$. Because our simulations are performed at $T = 0$, there is no thermal activation over the barriers on experimental time scales. Instead, the barriers can be overcome only due to increase

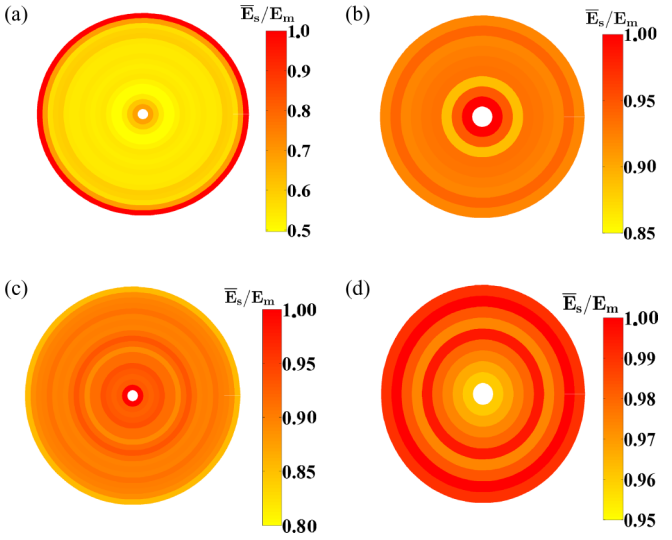

FIG. 9. Pictorial representation of Figs. 8(a)–8(d) showing the average heat dissipation in concentric spherical shells for (a) $a =$ 10 nm, $H_o = 0.4$ T, $f = 10^7$ Hz; (b) $a = 20$ nm, $H_o = 0.4$ T, $f = 10^7$ Hz; (c) $a = 10$ nm, $H_o = 0.4$ T, $f = 10^9$ Hz; and (d) $a = 20$ nm, $H_o = 0.4$ T, $f = 10^9$ Hz. The innermost shell with averaging $<10^3$ has been left blank in each of the pictographs.

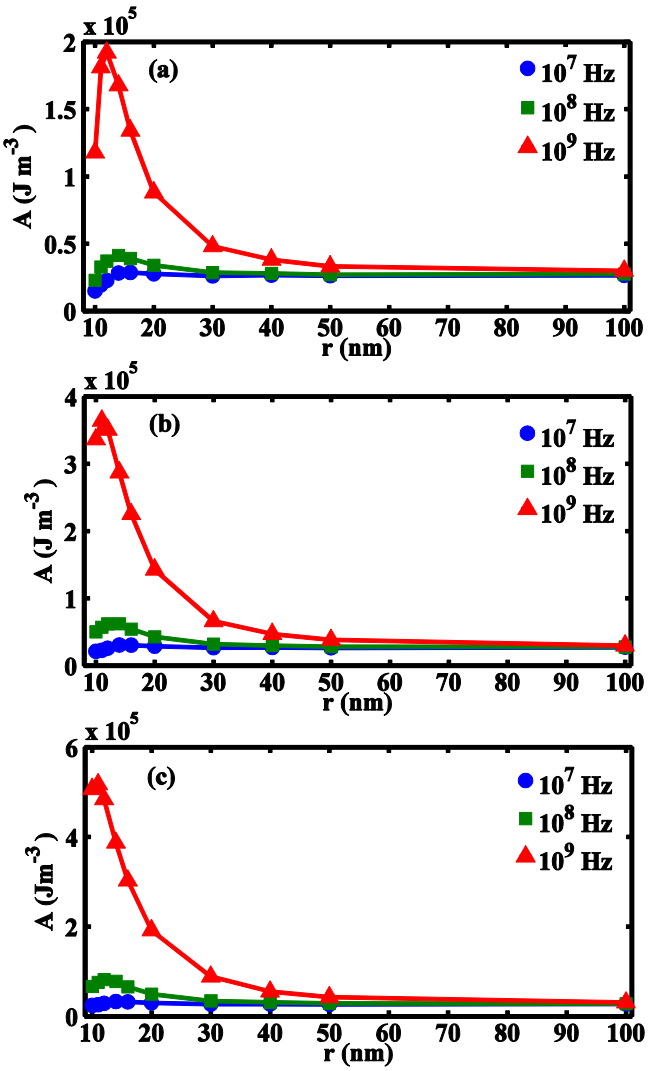

FIG. 10. Variation of the hysteresis loop area as a function of center-to-center interparticle separation a for cubic particles ($l = 10$ nm) of Fe_3O_4 assembled in a sphere ($R = 200$ nm). The rescaled amplitude H_o of the applied field is (a) 0.2, (b) 0.4, and (c) 0.6 T. Each set contains evaluations for three values of the frequency $f = 10^7$, 10^8, and 10^9 Hz. All data have been averaged over 50 initial conditions. Maximum heat dissipation is observed at a critical separation a^* and not at $a = l$ which maximizes the dipolar strength.

or decrease of the applied field. A magnetic moment becomes unstable when $|H(t)| > |h_i^e|$ as the field is varied slowly. Our results, presented in Figs. 3 and 5, have demonstrated that the core moments and surface moments have distinct morphological features and ground-state energy distributions. The core spins experience a magnetic environment well captured by the *mean-field approximation* [13,14]. We can imagine these moments to be under the influence of a local *mean* effective field h^{MF}. For the peripheral moments, on the other hand, the energy and the corresponding local field h_i^e exhibit a wide variation spanning three orders of magnitude. We do not expect the mean-field approximation to be valid here. Therefore, while the core spins will become unstable at $|H(t)| > |h^{MF}|$, there is no such threshold for the moments at the periphery. Rather, a few isolated sites on (and near) the surface are likely to become unstable at any value of $H(t)$.

To conclude, we have studied spherical assemblies of MNPs by solving Landau-Lifshitz (LL) equations using the open-source software OOMMF [28]. Our main interest was to study spin morphologies and heat dissipation in these aggregates as a function of the dipolar strength. The latter in our formulation was manipulated by the interparticle separation, the strength being maximum for particles in contact. As OOMMF is intrinsically not designed for such a study, we adapted the procedure by introducing a scaling protocol to correctly produce the effects due to variation of the interparticle separation (or the dipolar strength). It yields physical insights on aggregates of MNPs, which are in agreement with corresponding results in the literature obtained using alternative procedures such as the kinetic Monte Carlo simulations (kMCS). The role of dipole-dipole interactions in aggregates of MNPs is being increasingly emphasized in recent studies. We therefore believe that our adaptation will be very valuable. The interplay between the *small* system size and the *long*-range dipole-dipole interactions imparts different features to the core and the peripheral magnetic moments of the assemblies. As a consequence, they exhibit novel morphologies, multiple relaxation time scales, and spatially dependent heating.

Our primary observations are as follows: (a) Dense assemblies exhibit strong dipolar effects which yield local magnetic order in the core but not on the surface, where moments are randomly oriented. (b) The probability distribution of the ground-state energy of surface spins exhibits a long high-energy tail, in contrast to small tails for the core spins. (c) There is a strong correlation between ground-state energy and heating on application of an oscillating magnetic field $h(t) = h_o \cos 2\pi f t$: the particles in the core heat uniformly, while those on the surface exhibit a wide range, from cold

to intensely hot. (d) Specific choices of h_o and f yield characteristic spatial heating, e.g., hot surface and cold core, or vice versa, uniform, etc. (e) For all values of h_o and f that we considered, heating was maximum at a specific interparticle separation or dipolar strength. We have compared our results with a few recent works emphasizing the role of dipole-dipole interactions. These studies are at $T \neq 0$, so the dynamics is also via thermally activated escape over the barrier. Our analysis of morphologies and spatial distribution of ground-state energies is novel. It provides a basis to understand the repartitioning of heat observed by us and by Tan *et al.* [21].

Analytical frameworks to describe dipolar systems are few and far between, and numerical simulations do not yield ground states due to the trapping of the system in deep local minima. Therefore the nonequilibrium dynamics with multiple relaxation time scales has not been captured satisfactorily so far by theoretical and computational methods. Our understanding of these small systems with long-range interactions is hence far from complete. We hope that the observations and ideas presented in this paper will motivate great interest by the wide community of scientists, technologists, and therapists in furthering our understanding of the ubiquitous magnetic nanoparticle aggregates.

ACKNOWLEDGMENTS

The authors acknowledge partial financial support from the Indo-French Centre for Advanced Scientific Research, India. M.A. and V.B. also acknowledge partial financial support from the Department of Science and Technology (DST), India. We thank Thomas Blon for fruitful discussions on OOMMF micromagnetic simulations.

[1] Q. A. Pankhurst, N. T. K. Thanh, S. K. Jones, and J. Dobson, J. Phys. D: Appl. Phys. **42**, 224001 (2009).
[2] C. A. Schutz, L. J. Jeanneret, H. Mueller, I. Lynch, and M. Riediker, Nanomedicine **8**, 449 (2013).
[3] C. Corot, P. Robert, and J. M. Idee, Adv. Drug Delivery Rev. **58**, 1471 (2006).
[4] D. Kechrakos and K. N. Trohidou, Phys. Rev. B **58**, 12169 (1998).
[5] R. Bustamante, A. Millán, R. Piñol, F. Palacio, J. Carrey, M. Respaud, R. Fernandez-Pacheco, and N. J .O. Silva, Phys. Rev. B **88**, 184406 (2013).
[6] S. K. Murthy, Int. J. Nanomedicine **2**, 129 (2007).
[7] J.-H. Lee, J.-T. Jang, J.-S. Choi, S. H. Moon, S.-H. Noh, J.-W. Kim, J.-G. Kim, II.-S. Kim, K. I. Park, and J. Cheon, Nat. Nanotechnol. **6**, 418 (2011).
[8] L. H. Reddy, J. L. Arias, J. Nicolas, and P. Couvreur, Chem. Rev. **112**, 5818 (2012).
[9] Q. Zhao, N. Chen, D. Zhao, and X. Lu, ACS Appl. Mater. Interfaces **5**, 11453 (2013).
[10] Xi Chen, S. Sahoo, W. Kleemann, S. Cardoso, and P. P. Freitas, Phys. Rev. B **70**, 172411 (2004).
[11] J. P. Wang, Proc. IEEE **96**, 11 (2008).
[12] J. Carrey, B. Mehdaoui, and M. Respaud, J. Appl. Phys. **109**, 083921 (2011).
[13] V. Singh and V. Banerjee, J. Appl. Phys. **112**, 114912 (2012).
[14] V. Singh and V. Banerjee, Appl. Phys. Lett. **98**, 133702 (2011).
[15] A. Jordan, R. Scholz, P. Wust, H. Fähling, J. Krause, W. Wlodarczyk, B. Sander, Th. Vogl, and R. Felix, Int. J. Hyperthermia **13**, 587 (1997).
[16] H. Kachkachi, A. Ezzir, M. Noguès, and E. Tronc, Eur. Phys. J. B **14**, 681 (2000).
[17] M. L. Plumer, J. van. Lierop, B. W. Southern, and J. P. Whitehead, J. Phys.: Condens. Matter **22**, 296007 (2010).
[18] K. De'Bell, A. B. MacIsaac, I. N. Booth, and J. P. Whitehead, Phys. Rev. B **55**, 15108 (1997).
[19] M. Hanzlik, C. Heunemann, E. H. Rötzler, M. Winklhofer, N. Petersen, and G. Fleissner, BioMetals **13**, 325 (2000).
[20] L. Yan, S. Zhang, P. Chen, H. Liu, H. Yin, and H. Li, Microbiolog. Res. **167**, 507 (2012).
[21] R. P. Tan, J. Carrey, and M. Respaud, Phys. Rev. B **90**, 214421 (2014).
[22] H. J. Elmers, J. Hauschild, H. Fritzsche, G. Liu, U. Gradmann, and U. Köhler, Phys. Rev. Lett. **75**, 2031 (1995).
[23] O. Petracic, X. Chen, S. Bedanta, W. Kleemann, S. Sahoo, S. Cardoso, and P. P. Freitas, J. Magn. Magn. Mater. **300**, 192 (2006).
[24] S. Bedanta and W. Kleemann, J. Phys. D: Appl. Phys. **42**, 013001 (2009).
[25] K. Hiroi, K. Komatsu, and T. Sato, Phys. Rev. B **83**, 224423 (2011).
[26] X. Chen, S. Bedanta, O. Petracic, W. Kleemann, S. Sahoo, S. Cardoso, and P. P. Freitas, Phys. Rev. B **72**, 214436 (2005).
[27] Q. A. Pankhurst, J. Connolly, S. K. Jones, and J. Dobson, J. Phys. D: Appl. Phys. **36**, R167 (2003).
[28] M. J. Donahue and D. G. Porter, Interagency Report NISTIR No. 6376 (NIST, Gaithersburg, MD, 1999), http://math.nist.gov/oommf/.
[29] D. Serentes, K. Simeonidis, M. Angelakeris, O. Chubykalo-Fesenko, M. Marciello, M. D. P. Morales, D. Baldomir, and C. Martinez-Boubeta, J. Phys. Chem. C **118**, 5927 (2014).
[30] F. Burrows, C. Parker, R. F. L. Evans, Y. Hancock, O. Hovorka, and R. W. Chantrell, J. Phys. D: Appl. Phys. **43**, 474010 (2010).
[31] D. Serentes, D. Baldomir, C. Martinez-Boubeta, K. Simeonidis, M. Angelakeris, E. Natividad, M. Castro, A. Mediano, D.-X. Chen, A. Sanchez, LI. Balcells, and B. Martínez, J. Appl. Phys. **108**, 073918 (2010).
[32] C. Martinez-Boubeta, K. Simeonidis, D. Serentes, I. Conde-Leborán, I. Kazakis, G. Stefanou, L. Pena, R. Galceran, L. Balcells, C. Monty, D. Baldomir, M. Mitrakas, and M. Angelakeris, Adv. Funct. Mater. **22**, 3737 (2012).
[33] C. L. Dennis, A. J. Jackson, J. A. Borchers, P. J. Hoopes, R. Strawbridge, A. R. Foreman, J. van Lierop, G. Grüttner, and R. Ivkov, Nanotechnology **20**, 395103 (2009).
[34] L. C. Branquinho, M. S. Carrião, A. S. Costa, N. Zufelato, M. H. Sousa, R. Miotto, R. Ivkov, and A. F. Bakuzis, Sci. Rep. **3**, 2887 (2013).
[35] D. F. Coral, P. M. Zélis, M. Marciello, M. D. P. Morales, A. Craievich, F. H. Sánchez, and M. B. F. V. Raap, Langmuir **32**, 1201 (2016).
[36] G. T. Landi, Phys. Rev. B **89**, 014403 (2014).
[37] C. Haase and U. Nowak, Phys. Rev. B **85**, 045435 (2012).

[38] S. Ruta, R. Chantrell, and O. Hovorka, Sci. Rep. **5**, 9090 (2015).
[39] R. W. Chantrell, N. S. Walmsley, J. Gore, and M. Maylin, J. Appl. Phys. **85**, 4340 (1999).
[40] M. P. Seymour, I. Wilding, B. Xu, J. I. Mercer, M. L. Plumer, K. M. Poduska, A. Yethiraj, and J. V. Lierop, Appl. Phys. Lett. **102**, 072403 (2013).
[41] C. C. Dantas and L. A. de Andrade, Phys. Rev. B **78**, 024441 (2008).
[42] J. E. Miltat and M. J. Donahue, *Numerical Micromagnetics: Finite Difference Methods, Handbook of Magnetism and Advanced Magnetic Materials* (Wiley, New York, 2007).
[43] T. Fischbacher, M. Franchin, G. Bordignon, and H. Fangohr, IEEE Trans. Magn., **43**, 2896 (2007).
[44] W. F. Brown: *Micromagnetics* (Interscience, New York, 1963).
[45] A. Aharoni, *Introduction to the Theory of Ferromagnetism*, 2nd ed. (Oxford Science, Oxford, 2000).
[46] R. C. O'Handley, *Modern Magnetic Materials: Principles and Applications* (Wiley, New York, 1999).
[47] S. Blundell, *Magnetism in Condensed Matter*, 1st ed. (Oxford University Press, Oxford, 2001).
[48] J. M. D. Coey, *Magnetism and Magnetic Materials* (Cambridge University Press, Cambridge, 2010).
[49] Richard P. Boardman, Ph.D. thesis, University of Southampton, 2015, http://www.southampton.ac.uk/∼rpb/thesis.pdf.
[50] W. T. Coffey, Y. P. Kalmykov, and J. T. Waldron, *The Langevin Equation : With Applications to Stochastic Problems in Physics, Chemistry and Electrical engineering*. World Scientific Series in Contemporary Chemical Physics, Vol. 14, 2nd ed. (World Scientific, Singapore, 2004).
[51] O. Chubykalo-Fesenko, U. Nowak, R. W. Chantrell, and D. Garanin, Phys. Rev. B **74**, 094436 (2006).
[52] R. F. L. Evans, W. J. Fan, P. Chureemart, T. A. Ostler, M. O. A. Ellis, and R. W. Chantrell, J. Phys.: Condens. Matter **26**, 103202 (2014).
[53] K. H. Fischer and J. A. Hertz, *Spin Glasses* (Cambridge University Press, Cambridge, 1991).
[54] *Spin Glasses and Random Fields*, edited by A. P. Young (World Scientific, Singapore, 1998).